applied sciences

MDPI

Article

Experimental Study on Small-Strain Shear Modulus of Unsaturated Silty-Fine Sand

Kai Yan [1], Yong Wang [1,*], Zhiyong Yang [2], Xianghua Lai [3] and Cheng Chen [1]

[1] State Key Laboratory of Geomechanics and Geotechnical Engineering, Institute of Rock and Soil Mechanics, Chinese Academy of Sciences, Wuhan 430071, China
[2] Academy of Railway Sciences Engineering Consult Co., Ltd., Beijing 100081, China
[3] Second Institute of Oceanography, MNR, Hangzhou 310012, China
* Correspondence: wangyong@whrsm.ac.cn

Abstract: The small-strain stiffness of soil is significant in the accurate prediction of the deformation caused by interactions between foundation soil and structures. Considering the whole range of small strain (10^{-6}~10^{-3}), a bending element-resonant column (BE-RC) combined test system was developed to conduct continuous tests on the shear modulus of unsaturated soil. Under the dehydration path, it was used to investigate the small-strain shear modulus of unsaturated silty-fine sand in Hangzhou Bay, China. The results show that the shear modulus under different net stresses and matrix suctions appeared to non-linearly decay with the increase in strain until stable values were reached at a large strain. At the beginning from the saturated state, the G_{max} value increased slowly with decreasing saturation and reached its maximum value at the optimum saturation $(S_r)_{opt}$; then, it rapidly decayed to the level in the saturated, once the saturation degree decreased to a level lower than $(S_r)_{opt}$. Additionally, an improved prediction model was proposed for the G_{max} of unsaturated sand, considering different saturations. Based on the mesoscopic evolution of internal pore water morphology and the variation in intergranular stress caused by capillary action, the variation in the G_{max} could be divided into three segments of saturation: the boundary effect stage, the transition stage and the unsaturated residual stage.

Keywords: unsaturated soil; sand; resonance column; bending element; small strain; shear modulus

Citation: Yan, K.; Wang, Y.; Yang, Z.; Lai, X.; Chen, C. Experimental Study on Small-Strain Shear Modulus of Unsaturated Silty-Fine Sand. *Appl. Sci.* **2022**, *12*, 8743. https://doi.org/10.3390/app12178743

Academic Editor: Roohollah Kalatehjari

Received: 10 July 2022
Accepted: 28 August 2022
Published: 31 August 2022

1. Introduction

In actual engineering, foundation soil is often unsaturated. There are significant differences in the mechanical behaviours of saturated and unsaturated soil. Saturation vibration in soils causes serious engineering problems, such as the cracking and settlement of roadbeds, dams, shallow foundations and other structures [1]. Soil strain is divided into three intervals according to size: very small strain ($\leq 10^{-6}$), small strain (10^{-6}~10^{-3}) and large strain ($>10^{-3}$) [2]. Large amounts of engineering monitoring data have shown that the soil strain around the foundation of a geotechnical structure under a normal working load is generally small, mostly being concentrated in 0.01~0.1%. This is almost in the small-strain range [3]. Therefore, it is necessary to study the small-strain characteristics of unsaturated soils. In geotechnical dynamic analysis and design (e.g., the prediction of soil deformation behaviour under seismic, blasting, traffic loads and soil–structure interactions), the soil dynamic shear modulus is one of the key dynamic parameters and its value must be reasonable to accurately predict the deformation of geotechnical structures under a dynamic loading condition [4,5].

At present, there are three main methods used to determine the small-strain dynamic characteristic parameters of soils, which are the resonant column (RC) method, the bending element (BE) method and the torsional cyclic loading method (TCL). For more than 50 years, RC devices have been successfully used in the field of soil dynamics [6–9] and they are considered the most reliable method in the determination of the shear modulus and damping

capacity in soils. In the USA, the RC technique has become the standard ASTM method [10]. However, it is worth noting that the strain range of soils in RC tests is 10^{-5}~10^{-3}. Shirley et al. [11] first applied the BE technique to the field of geotechnical engineering. Dyvik et al. [12] further developed the technique and compared the BE and RC testing techniques. Since then, the BE test has been widely used as a convenient and promising method to measure the maximum shear modulus G_{max} of soils [13–16]. Generally, the strain range of soils in the BE test is 10^{-6}. Based on RC and BE apparatus, extensive studies have been carried out to investigate the influences of saturation degree or matrix suction on the shear modulus of unsaturated soils. Amoroso et al. [17] studied the decay of shear modulus with strain in different types of soils; the results revealed that shear modulus of different soils all decreased with an increase in strain, but the decay rates of different soils are different. Cho and Santamarina [18] indicated that the G_{max} of clay continues to increase with increasing saturation through BE testing. Dong and Lu [19] studied the effect of saturation on the small-strain shear modulus of clay based on BE tests and they found that the G_{max} increases with a decrease in saturation and the increasing trend is obvious when the saturation is low. Dutta et al. [20] studied the effect of saturation on the dynamic shear modulus of clay by RC tests and the results showed that the shear modulus increases with increasing suction in unsaturated clay. The results of these studies indicate that there is a clear trend for G_{max} versus saturation in clay. However, the evolution of the shear modulus of sand has been observed to be different from clay. Hardin and Richart [21] studied the dynamic shear modulus of unsaturated sand based on RC tests and the results showed that the degree of saturation has a small effect on the small-strain shear modulus at a low confining pressure. Wu et al. [22] studied the effect of different saturation levels on the small-strain shear modulus of five fine-grained cohesionless soils based on RC tests and it was found that the small-strain shear modulus increases and then decreases with the increase in saturation. Mancuso et al. [23] studied the small-strain behaviour of unsaturated compacted sands by RC torsional shear tests and indicated that suction and soil configuration have significant effects on the small-strain behaviour of sand. Kumar and Madhusudhan [24] experimentally studied the small-strain G_{max} of sand with different saturations based on BE tests and found that the peak for the G_{max} appears at a certain saturation. Nyunt et al. [25] studied the effects of the initial matrix suction and net confining pressure on the small-strain stiffness of remoulded sand based on BE tests and the results showed that small-strain stiffness has a non-linear relationship with matrix suction under each value of net confining pressure. Khosravi et al. [26] measured variations in the small-strain G_{max} of unsaturated sand during hydraulic hysteresis based on BE tests and indicated that during the drying process, the G_{max} varied in an up-and-down manner with respect to matrix suction, ranging from zero to the residual conditions. From this, it can be seen that although the small-strain shear modulus of unsaturated sand has been investigated experimentally, the continuous measurement of dynamic shear modulus on one and the same sand specimen in the whole small-strain range of 10^{-6}~10^{-3} under a controlled suction condition was seldom achieved in previous studies, due to the limitations in different strain ranges of soil between RC and BE tests. Moreover, only the macroscopic peak phenomenon of the sand shear modulus has been revealed to vary with saturation, but there was almost no internal reason from the mechanisms to be illustrated clearly.

In this work, the Stokoe RC instrument was improved and combined with a BE system, which could be used to conduct continuous tests regarding the shear modulus of a specimen under different saturations in the whole small-strain range of 10^{-6}~10^{-3}. Then, the BE-RC test device was used to investigate the small-strain shear modulus of unsaturated silty-fine sand in the dehydration path and the correlation between the evolution law of the G_{max} and the internal particle–water–air interaction mechanism varying with saturation was also studied in detail.

2. BE-RC Combined Test Device

2.1. Improvement of Device Pedestal and Top Cap

To control the matrix suction in a soil specimen, the first task is to modify the original Stokoe RC pedestal. A ceramic plate with an air entry value of 500 kPa was embedded in the center of the pedestal, thus, allowing a high level of matrix suction to be applied to a specimen using the axis translation technique for unsaturated soil. A limber hole and circular grooves were set below the ceramic plate to ensure a smooth water flow. The area where the ceramic plate and the pedestal connected was bonded with epoxy resin and cementation was completed at room temperature conditions for 24 h. Two cylindrical holes were set in the center of the pedestal and the top cap to install the bending element-extension element (BE-EE) probes. During the installation process, to improve the waterproof performance, rubber rings were added and silicone grease was applied to the side walls of the BE-EE probes, which prevented water from entering and eroding the data lines connecting the BE-EE probes under high-pressure conditions. Figure 1 shows the improved RC pedestal and top cap. Figure 2 shows the structure diagram of the improved BE-RC pedestal.

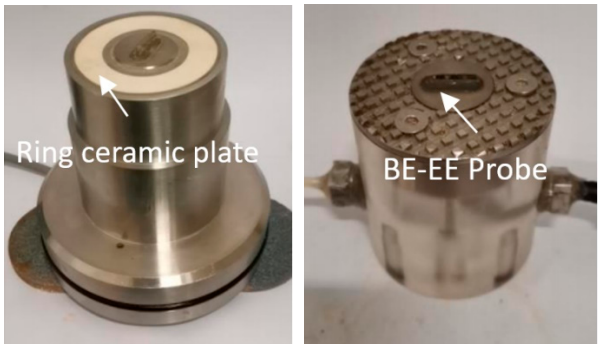

Figure 1. Photos of the reconstructed RC pedestal and top cap.

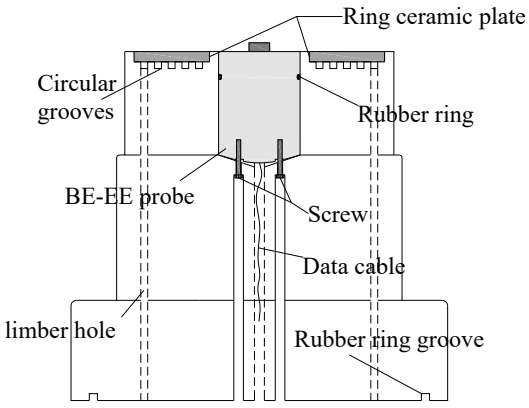

Figure 2. Schematic diagram of the improved RC pedestal.

Based on the modified RC pedestal and top cap, as shown in Figure 1, a test system combining a BE and RC was created. This system can allow the dynamic shear modulus of a soil specimen to be continuously tested in full range of small strains (10^{-6}~10^{-3}) under the dehumidification path by controlling the matrix suction.

2.2. Components in the Test System

In addition to an RC instrument controller, a BE controller, a confining pressure controller, a counterpressure controller, a data acquisition instrument and other components in the combined BE-RC test system, it was necessary to configure an air pressure controller in order to accurately control matrix suction. One channel of the air pressure controller was

connected to the original water outlet position of the RC top cap, enabling air pressure u_a to be applied to the inside of the specimen. Another channel connected to the confining pressure hole at the top of the pressure chamber, applying confining pressure p around the specimen. A back pressure controller was used to apply water pressure u_w to the specimen through the ceramic plate at the bottom of the specimen, as shown in Figures 3 and 4.

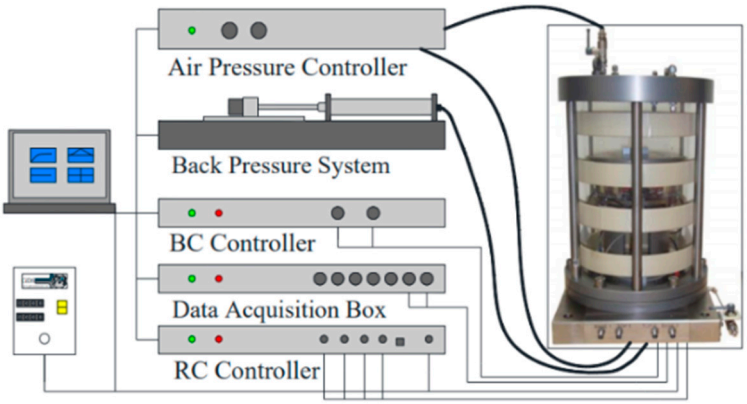

Figure 3. Schematic diagram of the general assembly of the unsaturated BE-RC test system.

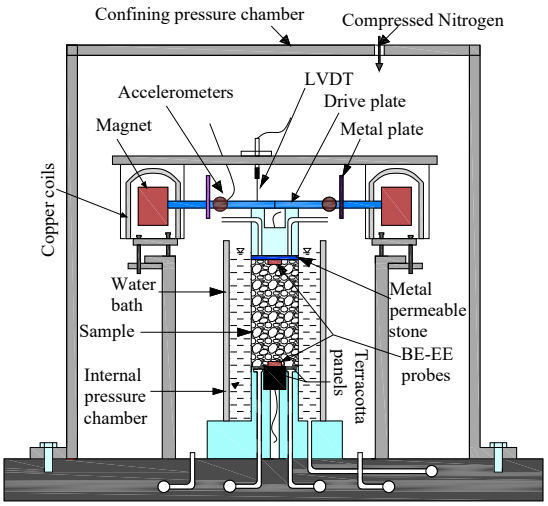

Figure 4. Schematic diagram of the configuration of the BE-RC unit.

The back pressure controller used in this work was a standard pressure/volume controller manufactured by GDS (Global Digtal System), which applies water pressure directly by driving a piston through a stepper motor and a screw actuator through a closed loop control. The volume change is measured by counting the number of steps in the stepper motor and it can be measured with an accuracy of 1 mm^3/kPa. To control the air pressure, a GDS dual-channel air pressure controller was adopted, which can simultaneously apply pore gas pressure and confining pressure to specimens with an accuracy of 1 kPa.

The improved combined unsaturated sand test system was based on the axis translation technique to control matrix suction. This was according to the definition of matrix suction, as shown in Equation (1):

$$\psi = u_a - u_w \tag{1}$$

where ψ is the matrix suction; u_a is the pore air pressure of the specimen; u_w is the pore water pressure of the specimen.

During the test, the specimen wrapped with latex film was placed on a ceramic plate. Air pressure u_a was applied inside the specimen and confining pressure p was applied outside the specimen using the air controller. Water pressure u_w was applied using the back

pressure controller. When the pore air pressure was greater than the pore water pressure, the pore water and gas moved in and out of the specimen until the specimen reached an equilibrium under the level of matrix suction ($\psi = u_a - u_w$). The net stress σ of the specimen was the difference between the confining pressure p and the pore air pressure u_a ($\sigma = p - u_a$). According to the suction equilibrium criterion, suggested by Pham [27], if the volume of drainage water was less than 0.1 cm^3 in a 24 h time interval, a suction equilibrium was deemed to have been reached. Then, the back pressure and pore air pressure valves were closed and the combined BE-RC tests were carried out.

2.3. Test System Calibration

Due to the installation of the BE-EE probe into the top cap of the RC, the structure and mass of the drive system in the Stokoe-type RC changed, resulting in a change in rotational inertia. Therefore, the rotational inertia I_0 of the drive system needed to be recalibrated. The calibration test method was to use three different-diameter calibration bars instead of the specimens and the shear modulus of the calibrated bars was known [28]. The calibration test results are shown in Figure 5. The rotational inertia value (I_0 = 0.003689) was obtained by taking the average value and subtracting the calibrated shim rotational inertia, which was applied to the experimental study of the shear modulus of unsaturated sand.

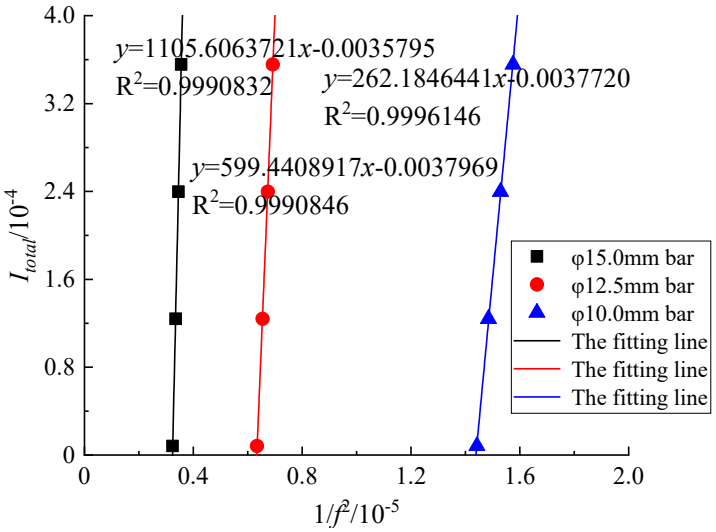

Figure 5. Calibration result of the unsaturated BE-RC test system.

2.4. Verification Test of the BE-RC Device

In order to test the reliability of the BE-RC test device, silty-fine sand from Hangzhou Bay in China was used to carry out a series of tests according to the standard ASTM method [29–32] and the basic physical parameters of the sand are shown in Table 1.

Table 1. The main physical parameters of silty-fine sand.

Specific Gravity	Minimum Dry Density (g/cm^3)	Maximum Dry Density (g/cm^3)	D_{50} (mm)	D_{10} (mm)
2.68	1.197	1.541	0.243	0.014

The head saturation method was used to saturate the prepared specimens. The back pressure was uniformly set to 50 kPa, the confining pressure was increased to 150 kPa, 250 kPa, 350 kPa and 450 kPa, respectively, and the consolidation was carried out for 12 h. Then, the BE and RC tests were carried out independently at different stress levels to complete tests on the saturated sand specimens. For each specimen, BE test was first

carried out, so the maximum shear modulus G_{max} could be measured. This was followed by an RC test. Due to the limitation of the test strain range, the RC test data were fitted using the Hardin-Drnevich equation and the back-calculation method to obtain the G_{max} of at the strain of 10^{-6}. The results of the BE and RC test measurements are compared in Figure 6.

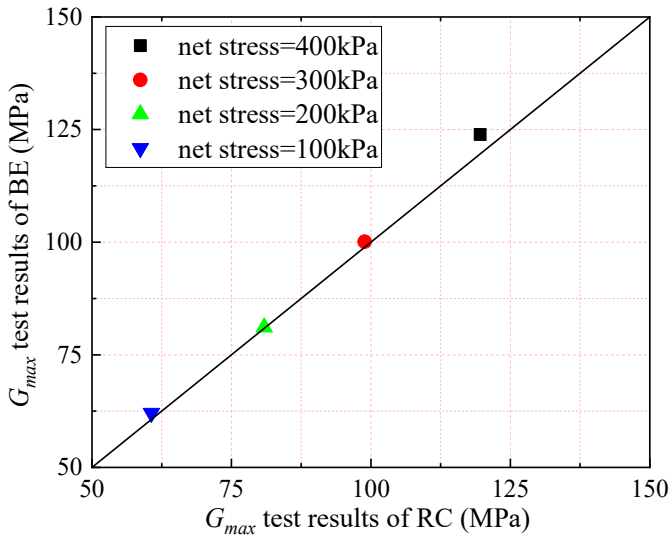

Figure 6. Comparison of G_{max} between the BE and RC test results.

Figure 6 shows that the BE test results agree well with the RC test results under different net stresses, with errors within 5%, indicating that the measurement performance of the improved BE-RC test system is reliable.

3. Small-Strain Tests for Unsaturated Sand

Small-strain shear modulus tests on unsaturated sands with different net stresses were conducted on silty-fine sand from Hangzhou Bay under the dehumidification stress path based on the improved BE-RC test device.

3.1. Test Program

Before the test, the soil–water characteristic curve (SWCC) for the silty-fine sand from Hangzhou Bay was measured with a pressure plate extractor and the experimental data were fitted using the Van Genuchten (VG) model, as shown in Figure 7 [33]. The saturation of a specimen was controlled by Equation (2):

$$S_r = S_c + \frac{(1 - S_c)}{\left[1 + (\alpha\psi)^n\right]^m} \quad (2)$$

where ψ is the matrix suction; S_r is the saturation; a, m and n are model parameters (a = 0.234, m = 0.116 and n = 0.234); S_c is the residual saturation (S_c = 0.172).

According to the relationship between saturation and matrix suction obtained from Equation (2), under the condition of keeping the net stress constant, we could obtain specimens with different saturation by controlling the matrix suction. Then, the combined BE-RC test on sand specimens under the dehumidification path was conducted and the correspondence between matrix suction and saturation during the test is shown in Table 2.

Table 2. Correspondence between matrix suction and saturation.

Matrix suction (kPa)	4	6	8	10	15	40	200	495
Saturation (%)	92	65	50	40	30	20	17	13

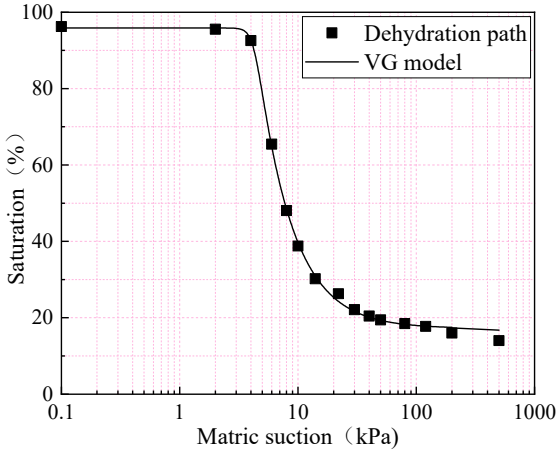

Figure 7. Prediction SWCC curve of VG model.

3.2. Test Method

During the preparation of the unsaturated sand specimen (ϕ50 mm × 100 mm, ρ_d = 1.337 g/cm^3), the ρ_d was consistent with that used in the previous SWCC test. Firstly, a sand sample with 5% water content was prepared by mixing oven-dried sand and air-free water; then, the sample was put in a sealed container for 12 h to make the moisture uniform. The sand specimen is formed with five layers of the sample in a saturator using the vibrating and tamping method and the surface was carefully scarped before the construction of the next layer, to strengthen the connections between the layers. The specimens were placed into a vacuum cylinder and saturated by the vacuum saturation method. As the saturated sand specimen could to be disturbed very easily, it was frozen first and then installed on the improved BE-RC pedestal. The back pressure was maintained at 50 kPa and the net stress of the specimen was maintained at 100 kPa. After the specimen was thawed, based on the axis translation technique, the confining pressure was set to 150 kPa, the pore air pressure was 50 kPa and the pressurization time was uniformly set to 120 min. The BE test was carried out first on the saturated sand specimen, followed by the RC test, to determine parameters, such as the shear wave velocity and shear modulus of the sand under different strains. After this, different levels of matrix suction were applied step by step, according to Table 2. The net stress and back pressure of the specimen remained unchanged and the pore air pressure and confining pressure changed based on the axial translation technique. When the suction equilibrium criterion was reached, the BE test was carried out first, followed by the RC test. Following the same method, small-strain shear modulus tests were conducted on unsaturated sand at net stresses of 200 kPa, 300 kPa and 400 kPa, respectively.

4. Shear Modulus of Sand with Different Saturations

The shear modulus G is an important parameter in the characterization of the dynamic properties of soil. Normally, when the shear strain γ exceeds a certain threshold ($\gamma > 10^{-5}$), the shear modulus of soil decays with the increase in shear strain. There are many factors that affect the decay characteristics in the dynamic shear modulus of soil and this study is mainly focused on the influences of saturation and net stress on the dynamic shear modulus of sand.

4.1. The Effect of Saturation on Dynamic Shear Modulus G

Using the previously developed BE-RC test device, the dynamic shear modulus G of the silty-fine sand in the whole small-strain range in the dehumidification stress path was obtained by controlling different net stresses and matrix suction states, as shown in Figure 8. Figure 8 shows the variation curve for shear modulus G with the shear strain for sand at different saturations, where the scattered points are the measured values and the solid lines are the fitted values using the Hardin-Drnevich model [6].

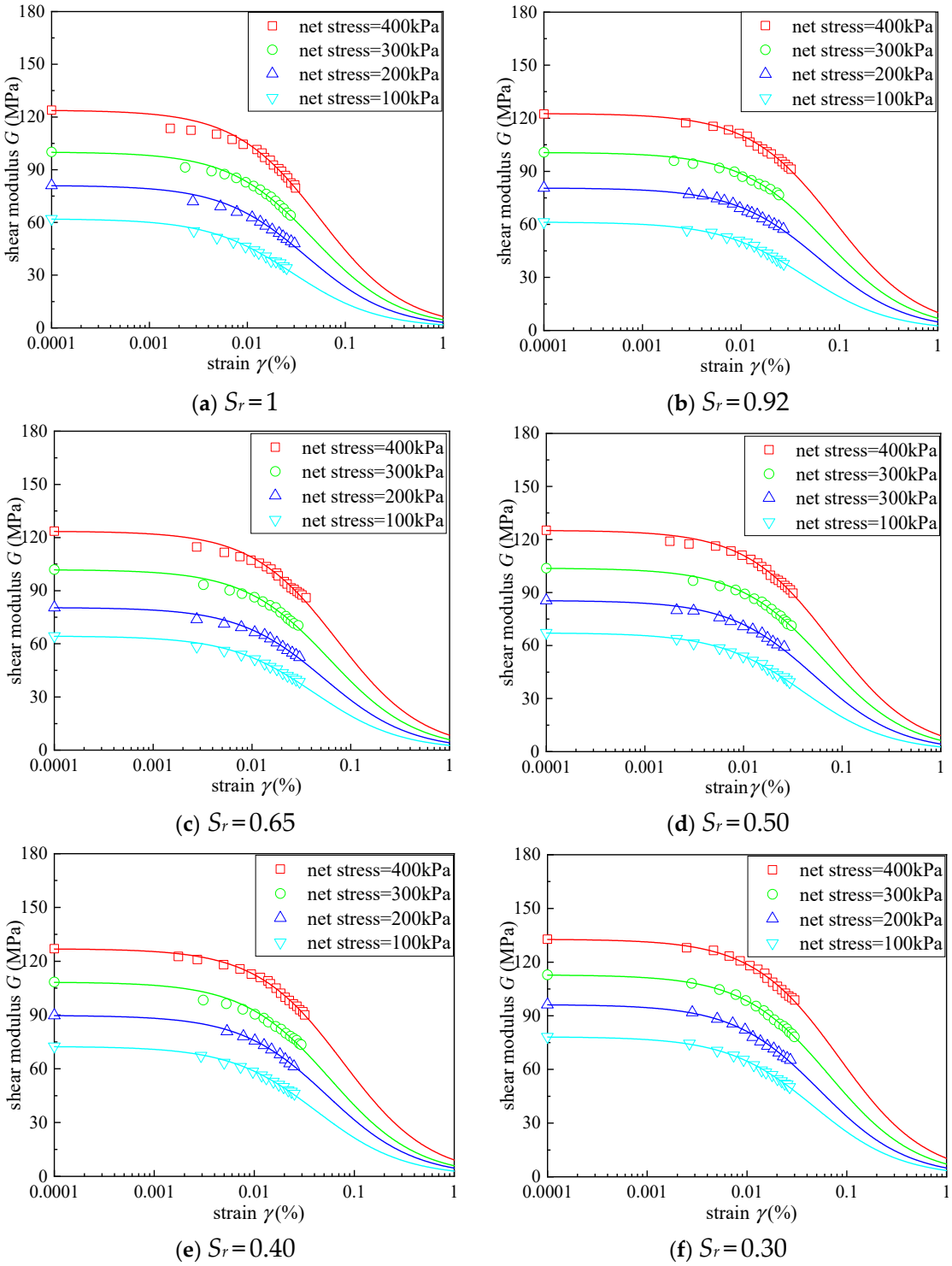

(**a**) $S_r = 1$ (**b**) $S_r = 0.92$

(**c**) $S_r = 0.65$ (**d**) $S_r = 0.50$

(**e**) $S_r = 0.40$ (**f**) $S_r = 0.30$

Figure 8. *Cont.*

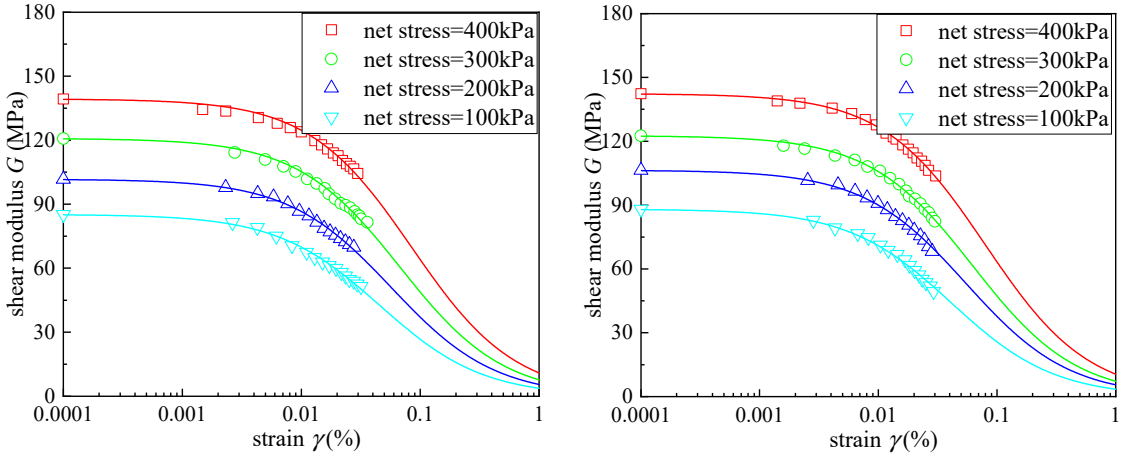

(**g**) $S_r = 0.20$ (**h**) $S_r = 0.17$

Figure 8. Relationship between shear modular G and shear strain γ for specimens at different saturations:(**a**) S_r = 1; (**b**) S_r = 0.92; (**c**) S_r = 0.65; (**d**) S_r = 0.50; (**e**) S_r = 0.40; (**f**) S_r = 0.30; (**g**) S_r = 0.20; (**h**) S_r = 0.17.

As shown in Figure 8, comparing the shear modulus curves of sand with the same saturation at different net stress levels, it can be found that the trend of decay in the dynamic shear modulus varies in the whole small-strain interval (10^{-6}~10^{-3}). When the strain is in a range of 10^{-6}~10^{-5}, the sand is basically in the linear elastic stage and the change in the shear modulus is not significant; when the strain is in a range of 10^{-5}~10^{-3}, the sand is in the elastoplastic stage and the shear modulus shows an obvious and rapid decrease; when the shear strain exceeds 10^{-3}, the sand is in the plastic stage and the shear modulus tends to level off [34]. The higher the initial net stress level, the larger the dynamic shear modulus G and the more significant the decay with the developing strain. Under the dehumidification path, the shear modulus G corresponding to the same strain does not vary monotonically with saturation. The maximum shear modulus G_{max} varies less with decreasing saturation at a higher saturation ($S_r \geq 0.4$). With a further decrease in saturation, the G_{max} increases gradually and reaches a peak at the saturation near 17%. This illustrates that: the matrix suction caused by saturation variation has a weak effect on the dynamic shear modulus of the sand at a higher saturation level; however, as the saturation decreases, the matrix suction increases and the ability of the sand to resist shear deformation increases, resulting in a slow increase in shear modulus G. However, a peak exists at a certain saturation.

4.2. The Effect of Saturation on G/G_{max}~γ

The Hardin-Drnevich hyperbolic model was used to normalize the G~γ decay curve to obtain the G/G_{max}~γ relationship curve. To investigate the effect of saturation on the decay characteristics of shear modulus with shear strain, the G/G_{max}~γ curves at different net stresses (100 kPa, 200 kPa, 300 kPa and 400 kPa) with different saturations (0, 0.17, 0.4, 0.65 and 1) were selected and summarized, as shown in Figure 9.

Figure 9a–d show that the normalized modulus G/G_{max} decreases with increasing shear strain and the smaller the net stress, the faster the decay in the modulus with strain. At the same shear strain, the normalized modulus G/G_{max} is not monotonically related to the change in saturation and reaches a maximum at saturation near 17%. Under the same net stress condition, the G/G_{max}~γ decay curve gradually increases with the decrease in saturation and it decreases when the saturation is less than 17%. The G/G_{max}~γ decay curves for dry sand coincide with or are slightly higher than those of saturated sand (S_r = 1.0). It shows that the G/G_{max}~γ decay curve firstly rises and then falls in a certain range with the decrease in saturation under the dehumidification path. This means that with the increase in matrix suction caused by the decreasing saturation, the inhibitory effect

on the decay of the dynamic shear modulus of the sand reaches a maximum value at a certain characteristic water content state.

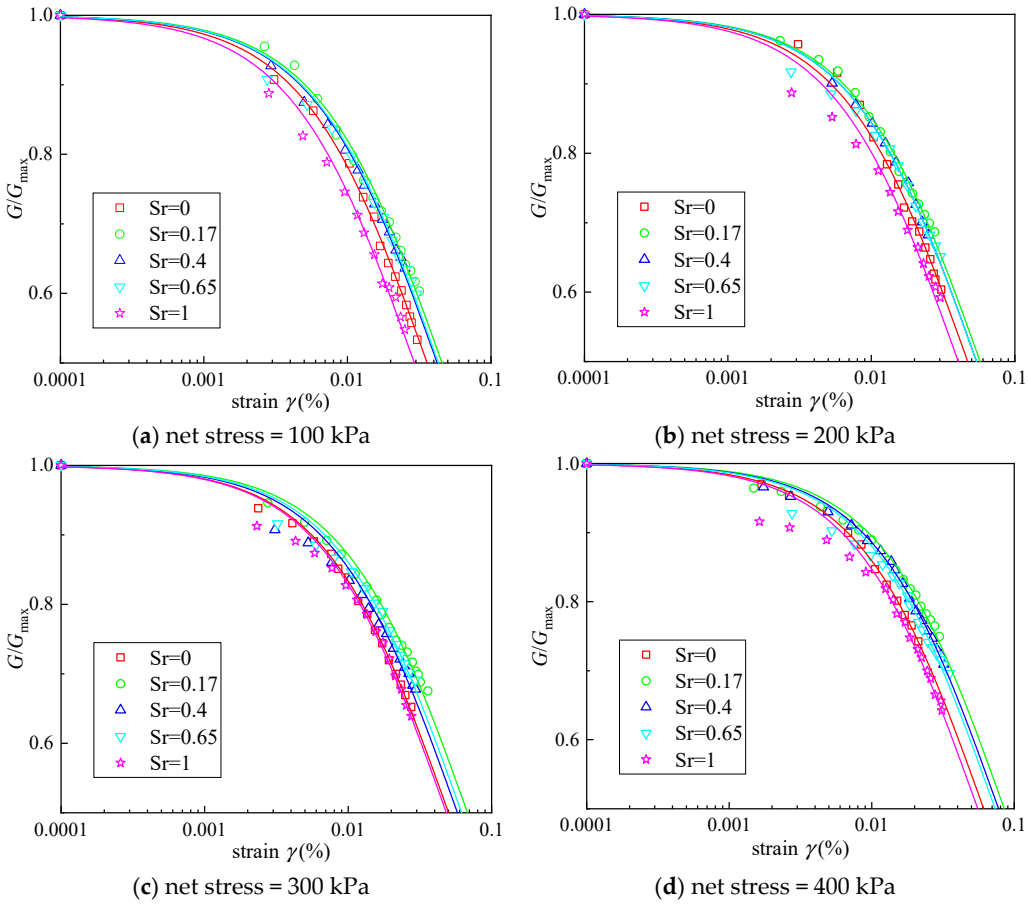

(**a**) net stress = 100 kPa (**b**) net stress = 200 kPa

(**c**) net stress = 300 kPa (**d**) net stress = 400 kPa

Figure 9. Relationship between G/G_{max} and shear strain at different net stress (**a**) 100 kPa; (**b**) 200 kPa; (**c**) 300 kPa; (**d**) 400 kPa.

4.3. The Relationship between G_{max} and S_r and the Prediction Model

It has been shown that the influence of confining pressure and the initial void ratio on the G_{max} is larger. Scholars have previously proposed empirical models to predict the G_{max} based on these two parameters [35–39]. The G_{max} generally decreases monotonically with the increase in saturation in clayey soils; in contrast, there is a threshold value for the G_{max} with increasing saturation in cohesionless soils. Wu et al. [22] studied the effect of capillary forces on the small-strain modulus of sand under different stresses and different saturation states based on RC tests and they found that the G_{max} gradually increases when the saturation is below a certain threshold, while the G_{max} decreases once the saturation exceeds the threshold, which is called the optimum saturation. They also proposed an empirical formula for determining the optimal saturation $(S_r)_{opt}$ based on the effective particle size D_{10}, as shown in Equation (3):

$$(S_r)_{opt} = -6.5 \log_{10}(D_{10}) + 1.5 \quad (3)$$

The particle size D_{10} for the silty-fine sand from Hangzhou Bay used in this work is 0.014 mm. Based on the calculation of Equation (3) and the optimal saturation in the silty-fine sand, we predicted ($(S_r)_{opt} \approx 13.55\%$). The measured G_{max}~S_r curve test showed that the saturation at the peak of the G_{max} is between 10% and 20%, which is generally

consistent with the findings of Wu et al. [22]. Additionally, a prediction model for the G_{max} considering the variation in saturation was given:

$$G_{max} = [1 + H(S_r)]G_{dry} \tag{4}$$

where $H(Sr)$ is a function of the saturation S_r, G_{dry} is the maximum shear modulus of the dry soil and $H(Sr)$ is defined as shown in Equation (5):

$$H(S_r)\begin{cases}(a-1)\sin\left(\frac{\pi S_r}{2b}\right) & S_r \le b\\ (a-1)F(S_r) & S_r > b\end{cases} \tag{5}$$

where a is the maximum value of the ratio of the maximum shear modulus of unsaturated soil to the maximum shear modulus of dry soil; b is the optimum saturation; and $F(S_r)$ is defined as shown in Equation (6):

$$F(S_r) = \frac{1}{2}\left(\frac{S_r - b}{100 - b}\right)^2 \cdot \sin\left\{\frac{\pi}{100 - b} \times \left[S_r + 50 - \frac{3}{2}b\right]\right\} \tag{6}$$

From Equation (5), it can be found that the prediction model is not continuous at the point of optimal saturation ($S_r = b$); the G_{max} at the optimum saturation converges to a times the value of the dry soil (i.e., $G_{max}(opt) \to aG_{dry}$) when the left side of the equation is closed to the optimal saturation; however, the G_{max} at the optimum saturation converges to the value of the dry soil (i.e., $G_{max}(opt) \to G_{dry}$) when the right side of the equation is close to the optimal saturation. Thus, in order to solve the discontinuity, $F(S_r)$ is proposed to be modified in Equation (7):

$$F(S_r) = \left(1 - \frac{S_r - b}{100}\right)^2 \cdot \sin\left\{\frac{\pi}{100 - b} \times \left[S_r + 50 - \frac{3}{2}b\right]\right\} \tag{7}$$

Equation (7) overcomes the problem of discontinuity in predicting the G_{max} of sand with different saturations by Equation (4). Thus, the G_{max} of silty-fine sand from Hangzhou Bay tested was predicted, as shown in Figure 10, where the solid line is the predicted value and the scatter point is the test value.

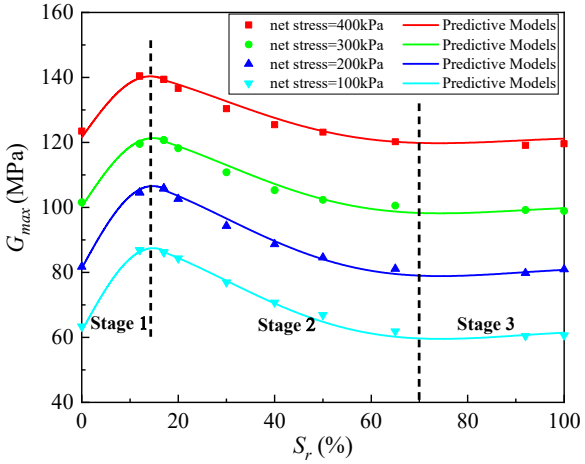

Figure 10. The prediction of G_{max} under different net stresses, Stage 1: unsaturated residual stage; Stage 2: transition stage; Stage 3: boundary effect stage.

Figure 10 shows a comparison between the predicted G_{max} of the proposed model and the tested result. It can be seen that they are in good agreement and the variation trend of the G_{max} with saturation at different stress levels is almost similar; the G_{max} increases slowly from the steady state as the saturation decreases and reaches the maximum value at

the optimum saturation and decreases rapidly when the saturation becomes lower. Finally, the G_{max} of dry sand decays to almost the same level as that of saturated sand.

The fitted parameters under different net stresses were derived from the improved prediction model, as shown in Table 3. Furthermore, values of optimal saturation b were obtained as 13.98%, 14.63%, 14.68% and 15.71% under the net stresses of 400 kPa, 300 kPa, 200 kPa and 100 kPa, respectively. This indicates that the optimal saturation of unsaturated sand tends to decrease as the net stress increases.

Table 3. The fit parameters of predictive model.

Parameter	σ = 400 kPa	σ = 300 kPa	σ = 200 kPa	σ = 100 kPa
a	1.131	1.195	1.305	1.364
b	13.98	14.63	14.68	15.71
R^2	0.98417	0.9869	0.9949	0.97877

Based on the distribution morphology of pore water and the internal force mechanism in sand particle aggregates under different saturations, the macroscopic G_{max}~S_r curves could be divided into three stages: the boundary effect stage, the transition stage and the unsaturated residual stage [40]. In the boundary effect stage (saturation of sand 100~70%), the capillary action has not yet appeared in sand particles with a decrease in saturation. In the transition stage (saturation 70~15%), the shear resistance property of sand is dominated by the capillary action and the combined force caused by the capillary action, which reaches the maximum value at optimum saturation. When the saturation further decreases to be lower than the optimum saturation, it enters the unsaturated residual stage, while the capillary action disappears and the short-range action force is activated. Here, the short-range action force refers to the combined force resulting from the action of the electric and van der Waals force fields near the solid–liquid interface.

Figure 11 is a schematic diagram of pore water distribution around particles. The structural water of a granular crystal has no effect on the interaction forces between particles under normal temperature conditions. The surface of a particle from near to far in order exists the strong adsorption water, the weak adsorption water, capillary water and pore gravity water. Adsorption water is primarily a water film attached to the particle surface, which is formed by the electrostatic gravitational force and the van der Waals force. The water film closest to the particle is subjected to adsorption forces up to several thousand atmospheres and its properties are similar to those of solids; the water film is called strong adsorption water. The remote layer of water film is called weak adsorption water, which is less affected by electro-molecular forces due to its distance from the particle. When the thickness of the weak adsorption water film reaches the maximum value, the redundant water forms a meniscus under the action of surface tension due to interaction between the water and air, thus, forming capillary water. Once the capillary water fills all the contact corners between granular particles until the curved liquid surface disappears, the excess water forms free-flowing gravity water, gradually filling all the remaining inter-particle pore space.

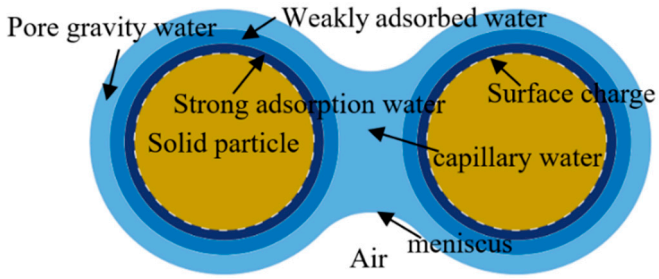

Figure 11. Schematic diagram of pore water distribution around sand particles.

The geometry of the meniscus between two equal-size particles can be described by the radius r_1 and r_2, the particle radius R and the filling angle θ, as shown in Figure 12a. Inter-particle force analysis is shown in Figure 12b. If the air pressure u_a is the only contribution to the external force, the intergranular stress F_e consists of three parts when the meniscus is formed. The total force generated by isotropic pore air pressure u_a acts at the gas–solid interface F_a, the projection of total force due to water pressure u_w acts on the water–solid interface in the vertical direction F_w and the combined force of surface tension γ acts on the circumference of the meniscus F_γ, described by Equations (8)–(11). The combined forces of capillary action F_{cap} consist of matrix suction and surface tension, as shown in Equation (12). Additionally, the intergranular stress F_e generated by the capillary phenomenon acts on particles in the form of tensile force [41,42].

$$F_a = u_a\left(\pi R^2 - \pi r_2^2\right) \tag{8}$$

$$F_w = u_w \pi r_2^2 \tag{9}$$

$$F_\gamma = -\gamma 2\pi r_2 \tag{10}$$

$$F_e = F_a + F_w + F_\gamma = u_a \pi R^2 - (u_a - u_w)\pi r_2^2 - \gamma 2\pi r_2 \tag{11}$$

$$F_{cap} = (u_a - u_w)\pi r_2^2 + \gamma 2\pi r_2 \tag{12}$$

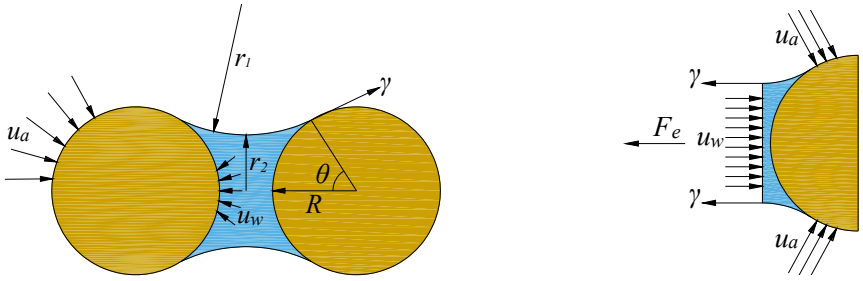

(**a**) (**b**)

Figure 12. Gas–liquid–solid interaction mode between two particles and meniscus:(**a**) sketch of interaction between two sand particles and meniscus; (**b**) illustration of inter-particle forces.

As can be seen from Figure 10, in the initial stage of the boundary effect (saturation 100~92%), the voids between sand particles are all filled with pore gravity water connecting to each other and there is only a small amount of air bubbles, which can freely flow with pore water. No capillary effect exists between the granular particles at this time; thus, the intergranular stress is unchanged. Only small changes in saturation occur and the G_{max} of sand is not affected. When the saturation of sand is gradually reduced from 92 to 70%, the pore gravity water in voids is displaced due to the entry of air. Although the curved liquid surface between the two phases of water–air is formed, the contact between the gas phase and the particle surface is not yet formed because the gravity water still exists around particles, while there is no effect of capillary action. Due to the fact that matrix suction causes little variation in intergranular stress, the ability of the particle system to resist shear deformation hardly changes; therefore, the G_{max} of sand remains unchanged. With a further reduction in saturation (from 70 to 15%), it enters the transition stage. The contact angle is formed with the solid particle–liquid–gas contact and capillary action is observed. According to Equations (8)–(12), although the surface tension action F_γ on the meniscus decreases with the decrease in the principal radius of curvature r_2, the matrix suction ψ gradually increases, leading to a gradual increase in the combined force of capillary action F_{cap}. This contribution to the intergranular stress F_e is enhanced, meaning the G_{max} of the sand begins to increase gradually. The intergranular stress reaches the maximum value when the curvature radius r_2 of residual capillary water meniscus in the contact areas of particles reaches the minimum value. At this time, the macroscopic saturation is at the

optimum saturation and the capability of sand to resist shear deformation reaches its peak. If the saturation is below the optimum saturation, it enters into the residual saturation phase. With the decrease in saturation, the capillary water, which only exists at corners near the particle contact point, disappears rapidly, meaning the combined force of capillary action F_{cap} is lost. Particles only connect through weak adsorption water. However, because the specific surface area of sand particles is small and the surface adsorption charge is lower, the adsorption water film of sand is very thin, meaning the weak adsorption water layer is also quickly lost. Although the distance between particles tends to be minimized and the interparticle short-range force could work, the distance between particles is still too large for sand particles, which is beyond the action range of the interparticle short-range force [43,44], resulting in a rapid reduction in the intergranular stress. Thus, the G_{max} of sand decays to a level being close to that in saturated sand.

5. Conclusions

In this work, based on an improved BE-RC test system for use in unsaturated soil, the small-strain shear modulus of unsaturated sand was investigated in the whole range of small strain (10^{-6}~10^{-3}) and the evolution law of the small-strain shear modulus and the internal particle–water–gas interaction mechanism, varying with the saturation level, are also elaborated upon using the dehumidification path. The main conclusions are as follows:

(1) In the range of small strain, with an increase in strain, the shear modulus of sand under different net stress levels gradually decays and tends to remain at a stable value under large strain. The higher the stress level, the faster decay of the shear modulus. At the same shear strain, the shear modulus of sand does not vary monotonically with the saturation but reaches the maximum value at optimum saturation.

(2) An improved prediction model for the G_{max} of sand considering saturation variation was proposed, by which the continuity problem in the model at the optimum saturation was solved.

(3) Based on the meso-scale morphological evolution of internal pore water in sand particles and the variation in intergranular stress caused by capillary action, the curve of G_{max} versus saturation was divided into three stages: the boundary effect stage, where saturation changes have almost no effect on the G_{max}; the transition stage, where capillary action plays a significant role and the G_{max} gradually increases with decreasing saturation and reaches a maximum at the optimum saturation; the unsaturated residual stage, where the intergranular stress rapidly decreases and the G_{max} decreases to the level in the saturation state.

Author Contributions: K.Y.; wrote the manuscript. Z.Y. and Y.W.; developed the BE-RC test system for unsaturated soils. K.Y. and X.L.; measured the soil–water characteristic curve of silty-fine sand in Hangzhou Bay, China. K.Y. and Z.Y.; performed the combined BE-RC tests. Y.W. and C.C.; wrote and edited the manuscript. All authors have read and agreed to the published version of the manuscript.

Funding: This research was funded by the NATURAL SCIENCE FOUNDATION OF CHINA, grant number 51979269 and 52127815.

Data Availability Statement: The data presented in this study are available on request from the corresponding author.

Conflicts of Interest: The authors declare that they have no conflict of interest.

References

1. Khosravi, A.; Ghayoomi, M.; McCartney, J.; Ko, H.Y. Impact of effective stress on the dynamic shear modulus of unsaturated sand. *GeoFlorida* **2010**, *199*, 410–419. [CrossRef]
2. Atkinson, J.H.; Sallfors, G. Experimental determination of stress–strain–time characteristics in laboratory and in situ tests. In Proceedings of the 10th European Conference on Soil Mechanics and Foundation Engineering, Florence, Italic, 26–30 May 1991; Volume 3, pp. 915–956.
3. Atkinson, J.H. Non-linear soil stiffness in routine design. *Géotechnique* **2000**, *50*, 487–508. [CrossRef]

4. Dong, Y.; Lu, N.; McCartney, J.S. Scaling shear modulus from small to finite strain for unsaturated soils. *J. Geotech. Geoenviron. Eng.* **2018**, *144*, 4017110. [CrossRef]
5. Ngoc, T.P.; Fatahi, B.; Khabbaz, H. Impacts of drying-wetting and loading-unloading cycles on small-strain shear modulus of unsaturated soils. *Int. J. Geomech.* **2019**, *19*, 4019090. [CrossRef]
6. Hardin, B.O.; Drnevich, V.P. Shear modulus and damping in soils: Measurement and parameter effects. *J. Soil Mech. Found. Div. ASCE* **1972**, *98*, 603–624. [CrossRef]
7. Drnevich, V.P. Resonant column testing: Problems and solutions. In *Dynamic Geotechnical Testing*; ASTM International: West Conshohocken, PA, USA, 1978; pp. 384–398. [CrossRef]
8. Saxena, S.K.; Avramidis, A.S.; Reddy, K.R. Dynamic moduli and damping ratios for cemented sands at low strains. *Can. Geotech. J.* **1988**, *25*, 353–368. [CrossRef]
9. Shibuya, S.; Tanaka, H. Estimate of elastic shear modulus in Holocene soil deposits. *Soils Found.* **1996**, *36*, 44–55. [CrossRef]
10. *ASTM Standard D4015*; Standard Test Method for Modulus and Damping of Soils by Fixed–Base Resonant–Column Method. ASTM International: West Conshohocken, PA, USA, 2015. [CrossRef]
11. Shirley, D.J.; Hampton, L.D. Shear-wave measurements in laboratory sediments. *J. Acoust. Soc. Am.* **1978**, *63*, 607–613. [CrossRef]
12. Dyvik, R.; Madshus, C. Laboratory measurements of G_{max} using bender elements. In Proceedings of the ASCE Annual Convention: Advances in the Art of Testing Soils under Cyclic Conditions, Detroit, MI, USA, 24 October 1985; pp. 186–196.
13. Sawangsuriya, A.; Edil, T.B.; Bosscher, P.J. Modulus-suction-moisture relationship for compacted soils. *Can. Geotech. J.* **2008**, *45*, 973–983. [CrossRef]
14. Truong, Q.; Lee, C.; Kim, Y.; Lee, J.S. Small–strain stiffness of salt–cemented granular media under low confinement. *Geotechnique* **2012**, *62*, 949–953. [CrossRef]
15. He, H.; Senetakis, K. A study of wave velocities and Poisson ratio of recycled concrete aggregate. *Soils Found.* **2016**, *56*, 593–607. [CrossRef]
16. Leong, E.; Cheng, Z. Effects of confining pressure and degree of saturation on wave velocities of soils. *Int. J. Geomech.* **2016**, *16*, D4016013. [CrossRef]
17. Amoroso, S.; Monaco, P.; Marchetti, D. Use of the Seismic Dilatometer (SDMT) to estimate in situ G–γ decay curves in various soil types. In *Geotechnical and Geophysical Site Characterization: Proceedings of the 4th International Conference on Site Characterization ISC–4*; Taylor & Francis Books Ltd.: Abingdon, UK, 2013; Volume 1.
18. Cho, G.C.; Santamarina, J.C. Unsaturated particulate materials–particle–level studies. *J. Geotech. Geo-Environ. Eng.* **2001**, *127*, 84–96. [CrossRef]
19. Dong, Y.; Lu, N. Correlation between small–strain shear modulus and suction stress in capillary regime under zero total stress conditions. *J. Geotech. Geoenviron. Eng.* **2016**, *142*, 4016056. [CrossRef]
20. Dutta, T.T.; Saride, S.; Jallu, M. Effect of saturation on dynamic properties of compacted clay in a resonant column test. *Geomech. Geoengin.* **2017**, *12*, 181–190. [CrossRef]
21. Hardin, B.O.; Richart, F.E., Jr. Elastic wave velocities in granular soils. *J. Soil Mech. Found. Eng. Div.* **1963**, *89*, 39–56. [CrossRef]
22. Wu, S.; Gray, D.H.; Richart, F.E., Jr. Capillary effects on dynamic modulus of sands and silts. *J. Geotech. Eng.* **1984**, *110*, 1188–1203. [CrossRef]
23. Mancuso, C.; Vassallo, R.; d'Onofrio, A. Small–strain behavior of a silty sand in controlled–suction resonant column torsional shear tests. *Can. Geotech. J.* **2002**, *39*, 22–31. [CrossRef]
24. Kumar, J.; Madhusudhan, B. Dynamic properties of sand from dry to fully saturated states. *Géotechnique* **2012**, *62*, 45–54. [CrossRef]
25. Nyunt, T.T.; Leong, E.C.; Rahardjo, H. Strength and small–strain stiffness characteristics of unsaturated sand. *Geotech. Test. J.* **2011**, *34*, 551–561. [CrossRef]
26. Khosravi, A.; Shahbazan, P.; Pak, A. Impact of hydraulic hysteresis on the small–strain shear modulus of unsaturated sand. *Soils Found.* **2018**, *58*, 344–354. [CrossRef]
27. Pham, H.Q. A Volume–Mass Constitutive Model for Unsaturated Soils. Ph.D. Thesis, University of Saskatchewan, Saskatoon, SK, Canada, 2005.
28. Wang, M.; Wang, Y.; Sun, M.; Wang, Y.; Sun, J. Development and preliminary application of resonant column–bending element combined testing apparatus. CAES2018. *IOP Conf. Ser. Earth Environ. Sci.* **2018**, *189*, 022084. [CrossRef]
29. *ASTM Standard D7928-21e1*; Standard Test Method for Particle–Size Distribution (Gradation) of Fine–Grained Soils Using the Sedimentation (Hydrometer) Analysis. ASTM International: West Conshohocken, PA, USA, 2021. [CrossRef]
30. *ASTM Standard D854-14*; Standard Test Methods for Specific Gravity of Soil Solids by Water Pycnometer. ASTM International: West Conshohocken, PA, USA, 2016. [CrossRef]
31. *ASTM Standard D4253-16e1*; Standard Test Methods for Maximum Index Density and Unit Weight of Soils Using a Vibratory Table. ASTM International: West Conshohocken, PA, USA, 2019. [CrossRef]
32. *ASTM Standard D4254-16*; Standard Test Methods for Minimum Index Density and Unit Weight of Soils and Calculation of Relative Density. ASTM International: West Conshohocken, PA, USA, 2016. [CrossRef]
33. Van Genuchcten, M.T. A Close–form equation for predicting the hydraulic conductivity of unsaturated soils. *Soil Sci. Soc. Am. J.* **1980**, *44*, 892–898. [CrossRef]
34. Jardine, R.J. Some observations on the kinematic nature of soil stiffness. *Soils Found.* **1992**, *32*, 111–124. [CrossRef]

35. Sawangsuriya, A.; Bosscher, P.J.; Edil, T.B. Application of soil stiffness gauge in assessing small–strain stiffness of sand with different fabrics and densities. *Geotech. Test. J.* **2006**, *29*, 207–216. [CrossRef]
36. Chien, L.K.; Oh, Y.N. Influence of fines content and initial shear stress on dynamic properties of hydraulic reclaimed soil. *Can. Geotech. J.* **2002**, *39*, 242–253. [CrossRef]
37. Saxena, S.K.; Reddy, K.R. Dynamic moduli and damping ratios for Monterey No.0 sand by resonant column tests. *Soils Found.* **1989**, *29*, 37–51. [CrossRef]
38. Iwasaki, T.; Tatsuoka, F. Effects of grain size and grading on dynamic shear moduli of sands. *Soils Found.* **1977**, *17*, 19–35. [CrossRef]
39. Afifi, S.S.; Richart, F.E., Jr. Stress–history effects on shear modulus of soils. *Soils Found.* **1973**, *13*, 77–95. [CrossRef]
40. Oh, W.T.; Vanapalli, S.K. Semi-empirical model for estimating the small–strain shear modulus of unsaturated non–plastic sandy soils. *Geotech. Geol. Eng.* **2014**, *32*, 259–271. [CrossRef]
41. Likos, W.J.; Lu, N. Hysteresis of capillary stress in unsaturated granular soil. *J. Eng. Mech.* **2004**, *130*, 646–655. [CrossRef]
42. Molenkamp, F.; Nazemi, A.H. Interactions between two rough spheres, water bridge and water vapour. *Geotechnique* **2003**, *53*, 255–264. [CrossRef]
43. Derjaguin, B.; Landau, L. Theory of the stability of strongly charged lyophobic sols and of the adhesion of strongly charged particles in solutions of electrolytes. *Prog. Surf. Sci.* **1993**, *43*, 30–59. [CrossRef]
44. Anandarajah, A.; Chen, J. Single correction function for computing retarded van der Waals attraction. *J. Colloid Interface Sci.* **1995**, *176*, 293–300. [CrossRef]